

Direct Reconstruction of Terahertz-driven Subcycle Electron Emission Dynamics

Jiakang Mao,^{1,2,*} Yushan Zeng,^{1,2,*} Hongyang Li,^{1,3} Liwei Song,^{1,2,†} Ye Tian,^{1,2,‡} and Ruxin Li^{1,2,4,§}

¹State Key Laboratory of Ultra-intense Laser Science and Technology, Shanghai Institute of Optics and Fine Mechanics (SIOM), Chinese Academy of Sciences (CAS), Shanghai 201800, China.

²Center of Materials Science and Optoelectronics Engineering, University of Chinese Academy of Sciences, Beijing 100049, China.

³School of Physics Science and Engineering, Tongji University, Shanghai 201210, China

⁴Zhangjiang Laboratory, Shanghai 201210, China

While field-driven electron emission is theoretically understood down to the subcycle regime, its direct experimental temporal characterization using long-wavelength terahertz (THz) fields remains elusive. Here, by driving a graphite tip with phase-stable quasi-single-cycle THz pulses, we reveal distinct subcycle electron emission dynamics including: (1) At a carrier-envelope phase (CEP) near zero, spectral peaks scale linearly with THz field strength, characteristic of subcycle emission; (2) At the opposite CEP, dominant deceleration fields generate stationary low-energy peaks. Crucially, we develop a pump-probe-free, direct reconstruction method extracting electron pulse profiles solely from measured energy spectra, obtaining durations from 97.3 to 114.3 fs as the field increases (191 – 290 kV/cm). Phase-resolved simulations further reveal a 71.2% modulation in the cutoff energy and a near-total (99.7%) suppression of the emission current. This work not only validates the Fowler-Nordheim model under THz excitation but also establishes a general framework for the direct temporal characterization of subcycle electron emission, opening pathways for precise electron control in ultrafast electron sources and lightwave nanoelectronics.

Ultrafast electron sources have become indispensable tools to probe matter at fundamental time and length scales, enabling breakthroughs across diverse areas including time-resolved electron microscopy [1], lightwave electronics [2], and coherent radiation sources [3,4]. A critical challenge in these applications lies in achieving precise control over electron emission and acceleration at subcycle timescales [5,6] – a regime that underlies strong-field phenomena [7,8] and delineates the quantum-to-classical transition during electron tunneling [9,10].

Recent advances in laser-driven electron emission have revealed rich dynamics ranging from multiphoton processes to field emission [11-13]. Quantitatively, their division is characterized by the Keldysh parameter [14] $\gamma = \sqrt{W/2U_p}$, where W is the work function, and U_p denotes the ponderomotive energy that is proportional to the laser intensity and the reciprocal of the angular frequency squared. As a result, $\gamma < 1$ (small ω and strong field regime) corresponds to quasistatic tunneling with the instantaneous currents implicitly assumed to be described by the Fowler-Nordheim (FN) model [15]:

$$I = \frac{A(\beta E_0)^2}{W} \exp\left(\frac{-BW^{3/2}}{\beta E_0}\right), \quad (1)$$

where I is the emission current, β is the field enhancement factor, E_0 is the incident optical field, constants $A = 1.56 \times 10^{-6} \text{ A V}^{-2} \text{ eV}$ and $B = 6.83 \times 10^9 \text{ V eV}^{-3/2} \text{ V m}^{-1}$.

The temporal characterization of ultrafast emission - a phenomenon essentially equivalent to the first step of the famous three-step model [16] in strong field physics - faces inherent difficulties due to the spectral overlapping of photoelectrons. Particularly, in uniform fields, direct energy-to-time mapping is inhibited by the nonmonotonic photoelectron spectra as well as the trajectory degeneracy where 'short' and 'long' classical paths could yield identical final energies [17,18]. These constraints necessitate pump-probe techniques like attosecond streaking [7,19] and quantum trajectory selection [20,21] to temporally resolve phase-dependent contribution in high harmonic generation or photoelectron spectroscopy, which methods, however, demand exquisite spatiotemporal synchronization between the driving field and probe pulses.

For solid-state electron sources, nanostructured field emitters - particularly sharp nanotips - have emerged as promising platforms due to their ability to concentrate optical fields [22]. The spatial adiabaticity parameter $\delta = l_F/l_q$ further classifies

electron dynamics into distinct regimes [23]: (1) when $\delta \geq 1$, electron quiver amplitude l_q fall within the near-field decay length l_F , resulting in complex rescattering processes (quiver regime); (2) Otherwise, when $\delta < 1$, the spatial inhomogeneity of near fields naturally filters rescattering electrons, pushing dynamics deeper into the subcycle regime. This spatial-reliant effect creates conditions where electron spectra become dominated by direct electrons - a prerequisite for reliable temporal reconstruction.

Our work exploits the unique advantages of single-cycle, carrier-envelope phase (CEP) stabilized terahertz (THz) pulses for subcycle field emission studies. The long wavelength of the THz pulse ($\lambda \approx 185 \mu\text{m}$) enables deeper penetration into the subcycle regime through the $\delta \propto \omega^2$ scaling (ω is the optical frequency), while the single-cycle waveform guarantees isolated emission windows. Crucially, the THz near-field creates a monotonic energy-time mapping where earlier-emitted electrons experience stronger acceleration, which contradicts the conventional Simplemann scenarios [24]. This unique relationship, combined with suppressed rescattering in spatially decaying fields, enables direct reconstruction of emission temporal profiles from electron energy spectra.

While THz-driven subcycle emission [25] has been evidenced via asymmetric emission threshold with flipped field polarity [26] or the linear energy peak shift [27-29] with varying electric field strengths, unambiguous temporal dynamics have remained elusive. Here we address this issue through systematic investigation of graphite tip emission driven by intense single-cycle THz pulses. Our study reveals: First, highly phase-dependent emission characteristics show linear scaling at $\varphi = -0.18\pi$, whereas an unreported stationary low-energy peak remains at $\varphi = 0.80\pi$. Second, a direct time-domain characterization method reconstructs the temporal electron profiles, which validates the FN theory by demonstrating a pulse width varying from 97.3 fs to 114.3 fs with increasing field intensity. Third, a phase-resolved simulation demonstrates a remarkable 71.2% CEP modulation of electron cutoff energies and a near-total (99.7%) suppression of the emission current. These advances provide both fundamental insights into subcycle emission physics and practical tools for ultrafast electron control.

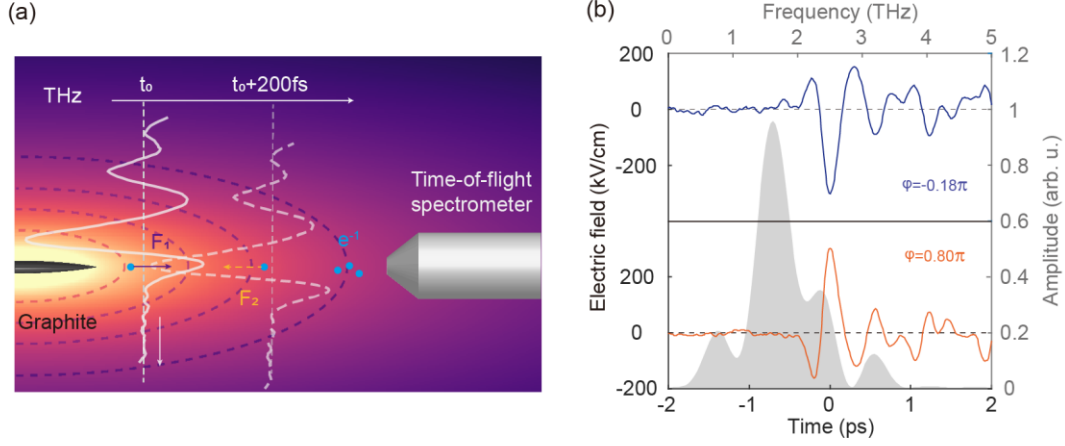


FIG. 1. THz-driven electron dynamics and field characterization. (a) THz-driven subcycle emission from a graphite tip: Negative THz half-cycle triggers electron emission (blue) and accelerates (purple F_1) electrons, while the positive half-cycle induces deceleration (yellow F_2). For low-energy electrons, the less confined inhomogeneous near-field causes sustained interaction with both THz half-cycles for hundreds of femtoseconds. (b) Measured THz waveforms via electro-optic sampling, with a peak field of 328 kV/cm and the corresponding Fourier spectrum shown in gray shading.

The investigation of subcycle electron emission dynamics requires control over the emission timing and acceleration fields with precise phase stability. As illustrated in Fig. 1(a) and Fig. S1 (see supplementary material for detailed experimental setup), our experimental setup achieves this control via employing quasi-single-cycle THz pulses generated in a DSTMS crystal [30,31]. Notably, the collinear optical rectification inside the crystal ensures inherent CEP stability while facilitating straightforward THz beam alignment. These pulses are subsequently focused onto a graphite tip in ultrahigh vacuum (1×10^{-5} pa), where they generate enhanced near-fields capable of driving electrons across the tunneling barrier within femtosecond timescales. The emitted electrons are characterized using a source meter (Keithley 6430) accompanied by a time-of-flight (TOF) energy spectrometer (Kaesdorf ETF10), with a static bias of -20 V maintained on the tip throughout measurements.

We first characterized the electron dynamics by their CEP-dependence of the emission yields as a function of THz electric field strength. By inverting the DSTMS crystal upside down, a decisive CEP phase shift between -0.18π and 0.80π is enabled which spans nearly half the THz cycle. The field polarity was determined via THz streaking [32,33] of the electrons (see supplementary material). Since the THz

waveform has a measured peak ratio of 0.53 between negative and positive half-cycles (see Fig. 1(b)), distinct electron emission thresholds were observed similar to the previous observation. As presented in Fig. 2(a), at $\varphi = -0.18\pi$, a stronger negative field dominates the emission field (see the purple arrow F_1 of Fig. 2(a)) which gives rise lower emission threshold of 137 kV/cm, whereas the $\varphi = 0.80\pi$ case exhibits a slightly higher value of 180 kV/cm as a result of weaker extracting electric field force F_2 (yellow arrow of Fig. 2(a)). Qualitatively, this process can be better described by a transformed Fowler–Nordheim equation of:

$$\ln\left(\frac{I}{E_0^2}\right) = \ln\left(\frac{A\beta^2}{W}\right) - \left(\frac{BW^{3/2}}{\beta}\right)\left(\frac{1}{E_0}\right), \quad (2)$$

which stipulates a linear scaling of the quantity $\ln(I/E^2)$ with the reciprocal of the applied electric field E . We verified this linear relation in Fig. 2(b), which provides a macroscopic field enhancement factor of $\beta \approx 24$, and $\delta \in [0.22, 0.47]$ for our THz field range of 137 to 290 kV/cm for $\varphi = -0.18\pi$.

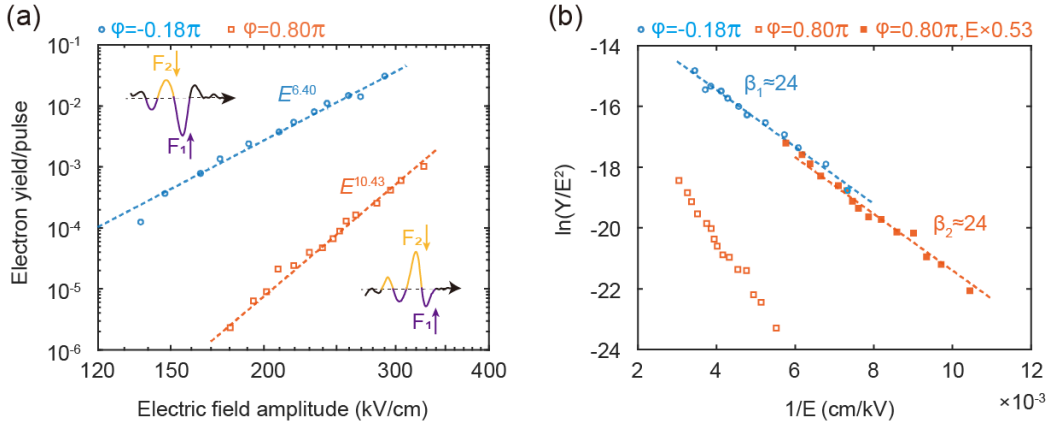


FIG. 2. Phase-dependent electron emission. (a) Measured electron emission yields as a function of the THz field strengths at $\varphi = -0.18\pi$ (exponent 6.40) and $\varphi = 0.80\pi$ (exponent 10.43). Insets: THz-waveform-driven electron acceleration (purple, F_1) and deceleration (yellow, F_2). (b) Fowler-Nordheim plot of the electron yields. The orange solid squares represent the field-scaled data of $\varphi = 0.80\pi$ (orange hollow squares) by the peak ratio of 0.53. The effective field enhancement factor is approximately 24 from numerical simulation.

Intuitively, a deeper insight into electron dynamics should incorporate the electron's kinetic energy because the time-accumulated action of the optical field could be (implicitly or explicitly) reflected in its final state. Hence, we next investigate the kinetic energies of these emitted electrons. The normalized spectral distributions are

presented in Figs. 3 (a) and (b) for $\varphi = -0.18\pi$ and $\varphi = 0.80\pi$, respectively. While their shapes both consist of a single peak with an extended pedestal, the two CEP cases exhibit stark contrasts in terms of peak position and the pedestal's extension directions. As demonstrated in Fig. 3 (c), the spectral peaks at $\varphi = -0.18\pi$ displayed linear scaling with THz field strength - a characteristic signature of subcycle emission. Conversely, at $\varphi = 0.80\pi$, a stationary low-energy peak was observed near 21.5 eV regardless of applied field intensity. The stationary peak is accompanied by a plateau-like high-energy pedestal, which, however, differs fundamentally from uniform-field photoelectron spectra.

To elucidate the physical origin of these spectral features, we numerically simulate electron tunneling and propagation including the static bias and the inhomogeneous near-field distributions. The electron trajectories were computed for sets of electrons with initial emission times dictated by the FN model and field settings derived from the experimental parameters. Further details of the simulation are provided in the supplementary material.

The simulations yield key spectral features of the experiment. In Figs. 3 (a) and (b), it is evident that the characteristic peak shifts in the experiment (blue solid lines) are well reproduced in the simulation (red dashed lines), while the calculated peak for $\varphi = 0.80\pi$ shows much narrower widths approaching 0.1 eV. To illustrate the result, we first provide a qualitative explanation of the unconventional anchored peak of the electron energy. While unfolding the final kinetic energy of an emitted electron as a function of its emission time (see Fig. S2), the spectrum is essentially a convolution of field-dependent tunneling probability with the acceleration dynamics. In the absence of (or with a weak) ensuing deceleration THz field such as at $\varphi = -0.18\pi$, the electron gains energy approximately proportional to the instantaneous field strength, thereby creating the stiff precipice at the high energy edge due to a maximal tunneling rate. However, when subsequent deceleration is strong, backward accelerations redistribute most electrons toward the detection threshold (which in our case is set mainly by the DC acceleration voltage), consequently forming anchored peaks. In this scenario, the observed extended pedestal at $\varphi = 0.80\pi$ stems from early emitted electrons as well as the late rescattering, while peak width discrepancies may originate from the THz energy jitter and our simplified model which neglected the electron's initial energy distribution and the electron-electron interactions.

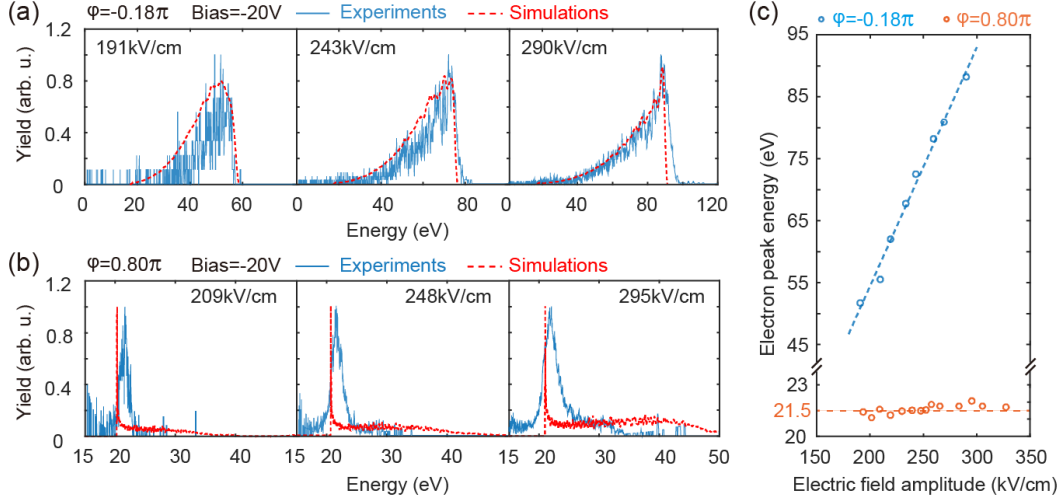


FIG. 3. Phase-dependent electron energy spectra. (a) Measured (blue) and simulated (red) spectra at $\varphi = -0.18\pi$ for THz field strengths of 191 kV/cm, 243 kV/cm, and 290 kV/cm. (b) Corresponding data at $\varphi = 0.80\pi$ for similar THz field strengths of 209 kV/cm, 248 kV/cm, and 295 kV/cm. The simulated electron spectra in (a) and (b) are presented with resolution matching the TOF's measurement precision. (c) Field-dependent peak energy scaling.

A further inspection of the time-energy mapping provides critical insights into the characteristic timescales governing subcycle electron dynamics. Figures 4(a) and (b) present a detailed view of simulated emission time versus final kinetic energy for $\varphi = -0.18\pi$ and $\varphi = 0.80\pi$, respectively. To extend the analysis beyond the experimentally accessible THz field amplitudes, we modulate the spatial adiabaticity parameter δ in simulations by varying the THz field strengths from 50 to 1000 kV/cm, with the experimental parameter range highlighted by the shaded area. Notably, two field-dependent effects emerge as δ decreases with increasing THz field strength: First, the emission time (phase) ϕ_0 corresponding to the maximum energy of directly emitted electrons progressively shifts towards the peak of the THz field (located at $t \approx 0$ for $\varphi = -0.18\pi$ and $t \approx -197$ fs for $\varphi = 0.80\pi$, where $t = 0$ denotes the THz envelope center). Second, the emission time of minimum energy is postponed, and the successive deceleration field could induce rescattering (colored dashed lines in Figs. 4(a) and (b)).

The peak shifts have direct implications for the spectral distributions. Specifically, at $\varphi = -0.18\pi$ (Fig. 4(a)), the emission time (ϕ_0) for maximum electron energy moves closer to $t = 0$ as the field intensity increases. Simultaneously, the slope of the

final kinetic energy versus emission time steepens near $t = 0$. These combined effects cause more electrons to concentrate at higher energies, resulting in the sharper high-energy spectral cutoffs observed experimentally in Fig. 3(a). In contrast, at $\varphi = 0.80\pi$ (Fig. 4(b)), rescattering processes dominate the highest energy portion of the spectrum. Notably, the peak positions of the direct electron energies stay distant from the THz field peak location, and the low-energy peak near $t \approx -197$ fs remains remarkably stable across our experimental THz field range. This stability directly accounts for the stationary spectral peak observed in Fig. 3(b).

The field-induced shifts in the energy-time mapping create a dynamic window exhibiting a monotonic dependence of final kinetic energy on emission time, which allows for direct reconstruction of temporal emission profiles from energy spectra. Crucially, the quasi-single-cycle nature of the THz waveform ensures a well-defined, isolated emission window. The case at $\varphi = -0.18\pi$ (shown conceptually in Fig.S2(a)) exemplifies this ideal condition for temporal reconstruction: as Fig. 4(c) illustrates, the monotonic energy-time correspondence enables a direct mapping over the range $[-28.7, 65.3]$ fs (colored shading), which captures the majority of emitted electrons.

Leveraging this mapping, we reconstructed the temporal electron emission profile directly from the experimental energy spectrum. The yellow data points in Fig. 4(d) represent this reconstructed profile. The full width at half maximum (FWHM) of the emission pulse was determined to be 114.3 (-5.9, +5.1) fs, demonstrating close agreement with the 114.9 fs prediction derived from the FN model.

Figure 4(e) reveals the dependence of the reconstructed pulse width on the applied THz field. As the THz field strength increases from 191 kV/cm to 290 kV/cm, the pulse width systematically broadens from 97.3 (-5.6, +3.1) fs to 114.3 (-5.9, +5.1) fs. This broadening is a direct consequence of the field-dependent tunneling probability described by the FN model: stronger fields not only increase the emission probability but also widen the characteristic emission time window. The error bars in Fig. 4(e) incorporate uncertainties arising from spectral fitting, laser energy fluctuations, and detection precision, underscoring the robustness of our reconstruction method.

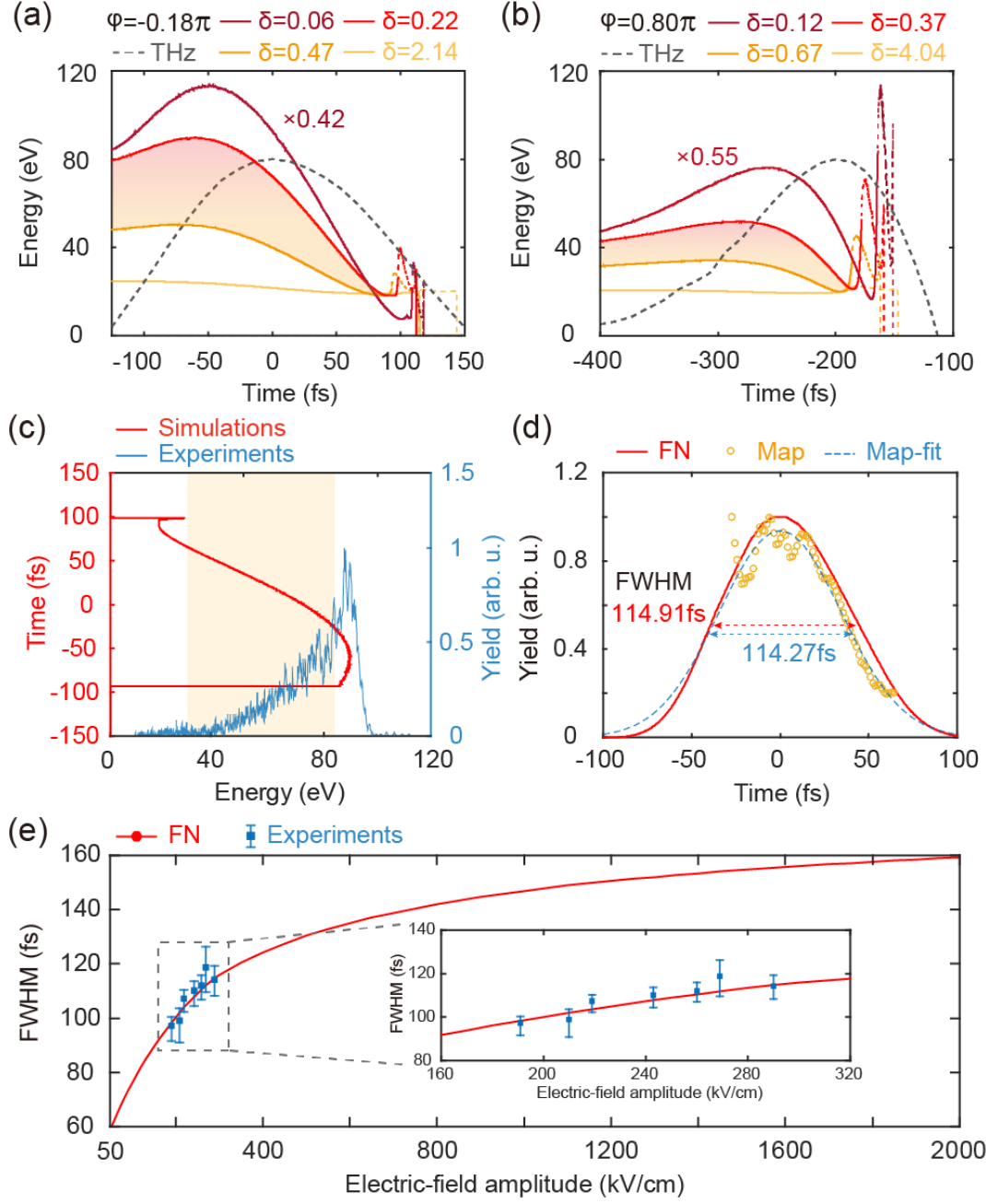


FIG. 4. Time-Energy Correlation of THz-Driven Electron Emission. (a) and (b), simulated final electron energy versus emission time. Solid and dashed colored lines denote direct and rescattering electrons, respectively, under different THz field strengths. The gray dashed line represents the THz electric field. The light red shaded region marks the experimental parameter range ($t = 0$: THz envelope center). (c) Simulated emission time-energy correlation (red) and detected electron energy spectrum (blue). (d) A mapping result of the electron emission profile with 290 kV/cm THz. (e) Mapped electron pulse widths (blue) are consistent with Fowler-Nordheim (FN) model predictions (red). The error bars include the energy jitter of our THz source, the fitting errors of the energy spectrum and the mapping process.

Relevantly, the peak shifts in Figs. 4(a) and (b) may at first glance appear like the delay of the emission phase of minimum energy while reducing the tip radii. In [34,35], this delay was explained in terms of near-field-induced electron trajectory asymmetry: Due to the inhomogeneous near field, a reduced initial acceleration phase is required to cancel out forward and backward acceleration. However, our intermediate δ range indicates additional breaking of time-reversal symmetry resulting from the quasi-single-cycle THz waveform. Particularly, the inherent temporal asymmetry of a single-cycle pulse prevents the vector potential of the THz field from returning to zero at zero-crossing [36]. When combined with spatial gradients (e.g., near the emission tips), these effects suppress rescattering, shift saddle points of energy-time correlation, and create complex phase-space filtering of electrons that produce the sloping-shaped and the peak-anchored energy spectra in Figs. 3(a) and (b), a feature not observed with multicycle pulses [34,37].

This strong phase dependence of electron emission is expected to significantly influence the final energy spectra. To comprehensively characterize this THz-field-dependent energy modulation, we simulated the energy spectra across varying CEP values (see THz waveforms in Fig. S3). Numerical simulations of CEP-modulated electron spectra in Fig. 5(a) confirm the strong CEP dependence of electron dynamics, with particularly pronounced effects contrasting $\varphi_{\text{CEP}} = 0$ and $\varphi_{\text{CEP}} = \pi$. The cutoff energy in Fig. 5(b), defined statistically as the energy below which 95% of the total electron population resides, exhibited a theoretical modulation depth of 71.2% at these two phases. Experimentally, this depth was measured as 57.1% at our applied CEPs, aligning well with the simulated value of 59.6%. The large contrast originates from the electron velocity evolution (Fig. 5(c)), where distinct deceleration for electrons emitted at $\varphi_{\text{CEP}} = \pi$ results in a minimum energy peak and a substantial 99.7% reduction in emission number. Since this emission energy and charge density modulation is singly reliant on the CEP, the observed high modulation depth demonstrates significant potential for precise, femtosecond-scale control of ultrafast electron pulses.

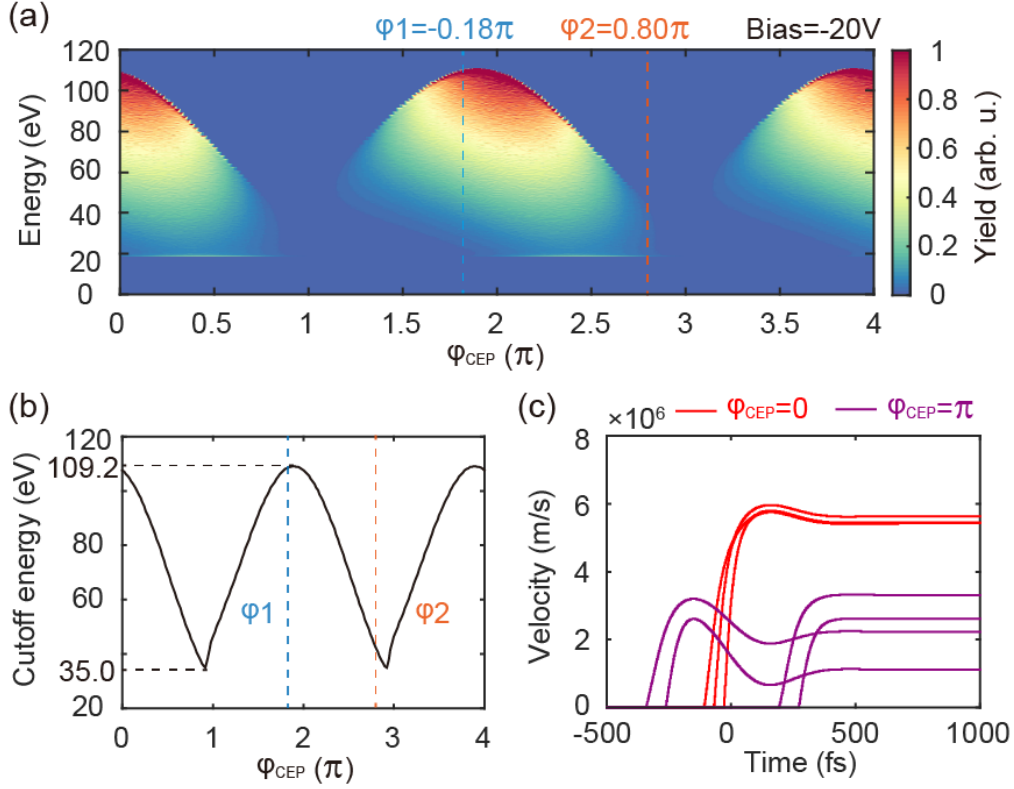


FIG. 5. CEP modulation of electron emission dynamics. (a) Simulated electron energy spectra as a function of THz CEP φ_{CEP} . Spectra corresponding to the experimental phases φ_1 (blue) and φ_2 (red) are indicated. (b) CEP-dependent high-energy cutoff, statistically defined as the energy below which 95% of the total electron population resides. The theoretical modulation depth reaches 71.2%. (c) Simulated electron velocity evolution profiles versus time delay within the spatially inhomogeneous near field, demonstrating distinct acceleration/deceleration behaviors dependent on the emission phase.

To sum up, our investigation of carrier-envelope-phase-stabilized, single-cycle terahertz-driven electron emission from a graphite tip reveals distinct phase-dependent dynamics critical for subcycle temporal characterization. At phase $\varphi = -0.18\pi$ which nears the zero CEP, linear scaling of spectral peak energy with THz field strength is observed, characteristic of subcycle emission governed by the FN model. Crucially, the THz near-field configuration at this phase establishes a monotonic mapping between electron kinetic energy and emission time, a direct consequence of the accelerating field profile where earlier-emitted electrons gain higher final energies. This unique relationship, enabled by the single-cycle waveform and suppressed rescattering in the inhomogeneous near-field, permits the direct reconstruction of the temporal emission profile solely from the measured energy spectrum. Applying this method, we

determined unambiguous subcycle emission pulse widths ranging from 97.3 fs to 114.3 fs as the THz field increased from 191 kV/cm to 290 kV/cm, corroborating the FN model predictions.

The subcycle emission is strongly influenced by the CEP. Aside from the stationary peak near 21.5 eV at $\varphi = 0.80\pi$, our phase-resolved simulations revealed a 71.2% modulation depth in electron cutoff energy. At higher driving THz fields, the emission is expected to penetrate deeper into the subcycle regime, enabling greater modulation depth and cutoff energy exceeding the keV range. Given the temporal demonstrates an optically driven, ultrafast electron source capable of delivering ~ 100 fs pulse widths with the majority of electrons concentrated in the high-energy region (see Fig. S4). We note that THz-driven electron emission exceeding the keV range has been previously reported [27-29,38]; the timescales of such electrons could be directly retrieved using our reconstruction approach.

The reconstruction approach could also be extended to other wavelengths beyond THz with a single emission window. Though the temporal resolution of this approach is approximately 8 fs in our experiment, we underscore the precision of this method is essentially constrained by three factors: (1) the energy resolution of the time-of-flight spectrometer; (2) The monotonic correlation window width; and (3) the data fineness of the measured energy spectrum. The error of our current experiment arises mainly from the third factor, which suffers from a coarse spectral curve due to a low collection efficiency of the TOF. However, the developed direct time-domain characterization method, leveraging energy-time mapping in tailored THz near-fields, establishes a powerful approach for femtosecond-scale temporal profiling and manipulation of electron pulses, with significant implications for advancing ultrafast electron sources and lightwave-driven nanoelectronics.

Acknowledgments-We are grateful to Zhinan Zeng from the Zhangjiang Laboratory, Songyu Zhu and Ruoyu Chen from SIOM for previous discussions. This work was supported by the National Key Research and Development Program of China (2022YFA1604400); National Natural Science Foundation of China (12325409, 12388102, U2267204); Shanghai Pilot Program for Basic Research, Chinese Academy of Sciences, Shanghai Branch, CAS Project for Young Scientists in Basic Research (YSBR-060).

*These authors contributed equally to this work.

[†]Contact Author: slw@siom.ac.cn

[‡]Contact Author: tianye@siom.ac.cn

[§]Contact Author: ruxinli@siom.ac.cn

References

- [1] D. Nabben, J. Kuttruff, L. Stolz, A. Ryabov, and P. Baum, Attosecond electron microscopy of sub-cycle optical dynamics, *Nature* **619**, 63 (2023).
- [2] M. Borsch, M. Meierhofer, R. Huber, and M. Kira, Lightwave electronics in condensed matter, *Nat. Rev. Mater.* **8**, 668 (2023).
- [3] D. Zhang, Y. Zeng, Y. Tian, and R. Li, Coherent free-electron light sources, *Photon. Insights* **2**, R07 (2023).
- [4] D. Zhang, Y. Zeng, Y. Bai, Z. Li, Y. Tian, and R. Li, Coherent surface plasmon polariton amplification via free-electron pumping, *Nature* **611**, 55 (2022).
- [5] X. Yu, Y. Zeng, L. Song, D. Kong, S. Hao, J. Gui, X. Yang, Y. Xu, X. Wu, Y. Leng, Y. Tian, and R. Li, Megaelectronvolt electron acceleration driven by terahertz surface waves, *Nat. Photonics* **17**, 957 (2023).
- [6] D. Zhang, A. Fallahi, M. Hemmer, X. Wu, M. Fakhari, Y. Hua, H. Cankaya, A.-L. Calendron, L. E. Zapata, N. H. Matlis, and F. X. Kärtner, Segmented terahertz electron accelerator and manipulator (STEAM), *Nat. Photonics* **12**, 336 (2018).
- [7] H. Y. Kim, M. Garg, S. Mandal, L. Seiffert, T. Fennel, and E. Goulielmakis, Attosecond field emission, *Nature* **613**, 662 (2023).
- [8] P. Dienstbier, L. Seiffert, T. Paschen, A. Liehl, A. Leitenstorfer, T. Fennel, and P. Hommelhoff, Tracing attosecond electron emission from a nanometric metal tip, *Nature* **616**, 702 (2023).
- [9] P. Dombi, Z. Pápa, J. Vogelsang, S. V. Yalunin, M. Siviš, G. Herink, S. Schäfer, P. Groß, C. Ropers, and C. Lienau, Strong-field nano-optics, *Rev. Mod. Phys.* **92**, 025003 (2020).
- [10] R. Bormann, M. Gulde, A. Weismann, S. V. Yalunin, and C. Ropers, Tip-Enhanced Strong-Field Photoemission, *Phys. Rev. Lett.* **105**, 147601 (2010).
- [11] B. Bánhegyi, G. Z. Kiss, Z. Pápa, P. Sándor, L. Tóth, L. Péter, P. Rácz, and P.

- Dombi, Nanoplasmonic Photoelectron Rescattering in the Multiphoton-Induced Emission Regime, *Phys. Rev. Lett.* **133**, 033801 (2024).
- [12] G. Hergert, R. Lampe, and C. Lienau, Quenching Strong-Field Rescattering of Photoemitted Electrons from Metallic Nanotapers by Using Moderate Bias Fields, *ACS Photonics* **12**, 2219 (2025).
- [13] J. Schötz, S. Mitra, H. Fuest, M. Neuhaus, W. A. Okell, M. Förster, T. Paschen, M. F. Ciappina, H. Yanagisawa, P. Wnuk, P. Hommelhoff, and M. F. Kling, Nonadiabatic ponderomotive effects in photoemission from nanotips in intense midinfrared laser fields, *Phys. Rev. A* **97**, 013413 (2018).
- [14] L. V. Keldysh, Ionization in the field of a strong electromagnetic wave, *J. Exp. Theor. Phys.* **20**, 1307 (1965).
- [15] R. H. Fowler, and L. Nordheim, Electron emission in intense electric fields, *Proc. R. Soc. Lond. A* **119**, 173 (1928).
- [16] P. B. Corkum, Plasma perspective on strong field multiphoton ionization, *Phys. Rev. Lett.* **71**, 1994 (1993).
- [17] D. Shafir, H. Soifer, B. D. Bruner, M. Dagan, Y. Mairesse, S. Patchkovskii, M. Y. Ivanov, O. Smirnova, and N. Dudovich, Resolving the time when an electron exits a tunnelling barrier, *Nature* **485**, 343 (2012).
- [18] N. Dudovich, O. Smirnova, J. Levesque, Y. Mairesse, M. Y. Ivanov, D. M. Villeneuve, and P. B. Corkum, Measuring and controlling the birth of attosecond XUV pulses, *Nat. Phys.* **2**, 781 (2006).
- [19] S. Brennecke, M. Ranke, A. Dimitriou, S. Walther, M. J. Prandolini, M. Lein, and U. Fröhling, Control of Electron Wave Packets Close to the Continuum Threshold Using Near-Single-Cycle THz Waveforms, *Phys. Rev. Lett.* **129**, 213202 (2022).
- [20] A. J. Piper, Q. Liu, A. Camacho Garibay, D. Kieseewetter, V. Leshchenko, J. E. Bækhoj, P. Agostini, K. J. Schafer, L. F. DiMauro, and Y. Tang, Attosecond Clocking and Control of Strong Field Quantum Trajectories, *Phys. Rev. Lett.* **134**, 073201 (2025).
- [21] K. J. Schafer, M. B. Gaarde, A. Heinrich, J. Biegert, and U. Keller, Strong Field Quantum Path Control Using Attosecond Pulse Trains, *Phys. Rev. Lett.* **92**,

023003 (2004).

- [22] D. Ehberger, J. Hammer, M. Eisele, M. Krüger, J. Noe, A. Högele, and P. Hommelhoff, Highly Coherent Electron Beam from a Laser-Triggered Tungsten Needle Tip, *Phys. Rev. Lett.* **114**, 227601 (2015).
- [23] G. Herink, D. R. Solli, M. Gulde, and C. Ropers, Field-driven photoemission from nanostructures quenches the quiver motion, *Nature* **483**, 190 (2012).
- [24] F. Krausz, and M. Ivanov, Attosecond physics, *Rev. Mod. Phys.* **81**, 163 (2009).
- [25] G. Herink, L. Wimmer, and C. Ropers, Field emission at terahertz frequencies: AC-tunneling and ultrafast carrier dynamics, *New J. Phys.* **16**, 123005 (2014).
- [26] S. Li, A. Sharma, Z. Márton, P. S. Nugraha, C. Lombosi, Z. Ollmann, I. Márton, P. Dombi, J. Hebling, and J. A. Fülöp, Subcycle surface electron emission driven by strong-field terahertz waveforms, *Nat. Commun.* **14**, 6596 (2023).
- [27] S. Li, and R. R. Jones, High-energy electron emission from metallic nano-tips driven by intense single-cycle terahertz pulses, *Nat. Commun.* **7**, 13405 (2016).
- [28] D. Matte, N. Chamanara, L. Gingras, L. P. R. de Cotret, T. L. Britt, B. J. Siwick, and D. G. Cooke, Extreme lightwave electron field emission from a nanotip, *Phys. Rev. Res.* **3**, 013137 (2021).
- [29] B. Colmey, R. T. Paulino, G. Beaufort, and D. G. Cooke, Sub-cycle nanotip field emission of electrons driven by air plasma generated THz pulses, *Appl. Phys. Lett.* **126**, 031108 (2025).
- [30] K. Wang, Z. Zheng, H. Li, X. Meng, Y. Liu, Y. Tian, and L. Song, Efficient strong-field THz generation from DSTMS crystal pumped by 1030 nm Yb-laser, *Appl. Phys. Lett.* **124** (2024).
- [31] Z. Zheng, K. Wang, H. Li, X. Meng, Y. Tian, and L. Song, High-repetition-rate strong-field terahertz source by optical rectification in DSTMS crystals, *High Power Laser Sci. Eng.* **12**, 05000e61 (2024).
- [32] L. Wimmer, G. Herink, D. R. Solli, S. V. Yalunin, K. E. Echternkamp, and C. Ropers, Terahertz control of nanotip photoemission, *Nat. Phys.* **10**, 432 (2014).
- [33] C. Kealhofer, W. Schneider, D. Ehberger, A. Ryabov, F. Krausz, and P. Baum, All-optical control and metrology of electron pulses, *Science* **352**, 429 (2016).

- [34] D. J. Park, B. Piglosiewicz, S. Schmidt, H. Kollmann, M. Mascheck, and C. Lienau, Strong Field Acceleration and Steering of Ultrafast Electron Pulses from a Sharp Metallic Nanotip, *Phys. Rev. Lett.* **109**, 244803 (2012).
- [35] D. J. Park, B. Piglosiewicz, S. Schmidt, H. Kollmann, M. Mascheck, P. Groß, and C. Lienau, Characterizing the optical near-field in the vicinity of a sharp metallic nanoprobe by angle-resolved electron kinetic energy spectroscopy, *Ann. Phys.* **525**, 135 (2013).
- [36] S. Li, and R. R. Jones, Ionization of Excited Atoms by Intense Single-Cycle THz Pulses, *Phys. Rev. Lett.* **112**, 143006 (2014).
- [37] B. Piglosiewicz, S. Schmidt, D. J. Park, J. Vogelsang, P. Groß, C. Manzoni, P. Farinello, G. Cerullo, and C. Lienau, Carrier-envelope phase effects on the strong-field photoemission of electrons from metallic nanostructures, *Nat. Photonics* **8**, 37 (2014).
- [38] J. Ying, X. He, D. Su, L. Zheng, T. Kroh, T. Rohwer, M. Fakhari, G. H. Kassier, J. Ma, P. Yuan, N. H. Matlis, F. X. Kärtner, and D. Zhang, High gradient terahertz-driven ultrafast photogun, *Nat. Photonics* **18**, 758 (2024).